https://eprints.gla.ac.uk/271617/

Deposited on: 24 May 2022

Accurate Quantum Transport Modelling of High-Speed In$_{0.53}$Ga$_{0.47}$As/AlAs Double-Barrier Resonant Tunnelling Diodes

Davide Cimbri[iD], Begüm Yavas-Aydin, Fabian Hartmann, Fauzia Jabeen, Lukas Worschech, *Member*,

IEEE, Sven Höfling, *Senior Member*, *IEEE*, and Edward Wasige[iD], *Member*, *IEEE*

Abstract— In this paper, we demonstrate a reliable physics-based simulation approach to accurately model high-speed In$_{0.53}$Ga$_{0.47}$As/AlAs double-barrier resonant tunnelling diodes (RTD). It relies on the non-equilibrium Green's function (NEGF) formalism implemented in SIL-VACO Atlas TCAD quantum simulation package to closely mimic the actual device physics, together with the judicious choice of the material parameters, models, and suitable discretisation of the associated epitaxial layer structure. The validity of the approach was proven by comparing simulated data with experimental measurements resulting from fabricated micron-sized RTD devices featuring two different epitaxially grown layer stacks. Our results show that the simulation software can correctly compute the peak current density J_p, peak voltage V_p, and the valley-to-peak voltage difference $\Delta V = V_v - V_p$ associated with the negative differential resistance region (NDR) of the RTD heterostructure static current density-voltage (*JV*) characteristic at room temperature (RT), all of which are key parameters in the design of these devices for use in oscillator circuits. We believe that this work will now help in optimising the RTD epitaxial structure to maximise its radio-frequency (RF) power performance, accelerating developments in the rapidly evolving RTD technology for emerging applications, including next-generation ultrabroadband short-range wireless communication links and high-resolution imaging systems.

Index Terms— Resonant tunnelling diode, double-barrier quantum well, non-equilibrium Green's function, current-voltage characteristic, negative differential resistance, low-terahertz oscillator.

I. INTRODUCTION

RESONANT tunnelling diodes (RTD) represent a promising candidate technology suitable to design emitters and detectors required by next-generation terahertz (THz) (0.1−10 THz) applications, including high-speed wireless communications [1] and high-resolution imaging [2]. However, the main limitation of this technology is represented by the low output power of the sources. Currently, indium phosphide (InP) RTD-based transmitters (Tx) have achieved output powers of up ∼ 1 mW in the 300 GHz-band [3], which have demonstrated short-range wireless communication with data rates of up ∼ 22 Gb/s along an ∼ 80 cm long data link [4]. Nonetheless, link budget estimations show that several mW of output power are required to both increase channel bandwidth by several tens of Gb/s and further extend the link distance to several metres, meeting the requirements needed for practical applications [5].

In this context, the diode maximum radio-frequency (RF) power $P_{RF,max}$ is intimately related with its static current-voltage (IV) characteristic, in particular, with the span of the negative differential resistance (NDR) region [6]. Since $P_{RF,max} \approx (3/16)\Delta I \Delta V$, where $\Delta I = I_p - I_v$ is the peak-to-valley current difference and $\Delta V = V_v - V_p$ the valley-to-peak voltage difference, an accurate estimation of both the available current density $\Delta J = \Delta I/A = J_p - J_v$ (being A the RTD mesa area) and ΔV is essential to maximise the device RF power, where peak and valley current densities J_p and J_v, and voltages V_p and V_v, represent a fingerprint of the RTD epitaxial structure.

The establishment of a clear device design methodology aimed at maximising $P_{RF,max}$ in the low-THz band ($\sim 100 - 300$ GHz) is yet to be developed and requires a reliable physics-based simulation approach capable of accurately predicting the electrical behaviour of the RTD device. Although few numerical simulation tools have been developed in the past [7]−[9], none of them has found practical applicability in this context. At the same time, those based on SILVACO Atlas TCAD were unclear, with missing or incomplete information about the employed physical models and material parameters [10]−[12]. Further, no accurate comparison between simulated and fabricated devices aimed at establishing the reliability of the software has been conducted so far.

In this work, we propose a reliable physics-based simulation method to accurately model high-speed In$_{0.53}$Ga$_{0.47}$As/AlAs double-barrier RTD devices. Our approach relies on the non-equilibrium Green's function (NEGF) formalism implemented in SILVACO Atlas TCAD quantum simulation package to accurately account for the physics of the device, as well as on the careful selection of the epitaxial layers material parameters, models, and appropriate discretisation of the RTD wafer structure.

The paper is organised as follows. Section II introduces to

Davide Cimbri and Edward Wasige are with the High-Frequency Electronics group, division of Electronics and Nanoscale Engineering, James Watt School of Engineering, University of Glasgow, G12 8LT, Glasgow, United Kingdom (e-mail: davide.cimbri@glasgow.ac.uk).

Begüm Yavas-Aydin, Fabian Hartmann, Fauzia Jabeen, Lukas Worschech, and Sven Höfling are with the Technische Physik, University of Würzburg and Wilhelm-Conrad-Röntgen-Research Center for Complex Material Systems, Am Hubland, D-97074, Würzburg, Germany.

the NEGF method aimed at RTD modelling, Section III describes the developed simulation approach and the experiment comparing the simulated with the fabricated and measured devices, while Section IV concludes with final remarks.

II. NON-EQUILIBRIUM GREEN'S FUNCTION METHOD

As discussed in the preceding section, an accurate estimation of the static JV characteristic of the RTD epitaxial structure is of key importance to carry out device design for RF power performance maximisation. Approximate semi-empirical analytical methods and standard numerical approaches based on the self-consistent solution of the single-electron Schrödinger's and Poisson's equations are widely employed to model the electrical properties of RTDs within the Landauer-Büttiker limit [13]−[15]. However, a complete quantum electron transport treatment based on kinetic models is preferred to treat carrier transport at a full quantum level and formally include strong many-body interactions that lead to a generalised mixed-state electron description [16], including electron-electron elastic scattering, and, more importantly, dissipative processes, such as electron-acoustic/optical phonon, alloy, impurity, and interface roughness-related inelastic scattering [17]. Indeed, a realistic RTD device is far from being a closed quantum environment described by a conservative Hamiltonian, but it can be considered as an open particles ensemble governed by the laws of non-equilibrium quantum statistical mechanics.

In this regard, the NEGF approach is considered among the most accurate methods to describe the process of carrier transport in nanoscale devices [18]. The electron wave-like nature is fully preserved and accounted in the NEGF formalism, treating electron transport at a fully quantum level, differently from classical drift-diffusion and Boltzmann transport equation (BTE)-based models [19]. Moreover, the inclusion of electronic wave-function phase decoherence mechanisms is straightforward and can be quantum-mechanically accounted through the concept of scattering self-energy [20], contrarily to conventional Monte Carlo approaches [21]. In this context, the electronic self-energy models the interaction between the electron and the surrounding environment. It would, therefore, seem that the NEGF method represents an appealing solution to accurately address the problem of modelling and simulation of the RTD device [22].

III. SIMULATION OF THE RTD EPITAXIAL STRUCTURE STATIC JV CHARACTERISTIC

A. Epitaxial structures

To establish a reliable simulation approach, the static JV characteristic of two epitaxial structures under test (ESUT) was first simulated in Atlas through the NEGF method. The ESUT were then epitaxially grown by molecular beam epitaxy (MBE) on InP substrates, after which RTD devices were fabricated and measured. Experimental results were then compared with simulations.

The n-type intraband RTD ESUT are depicted in Fig. 1. They consist of a lattice-matched to InP $In_{0.53}Ga_{0.47}As$
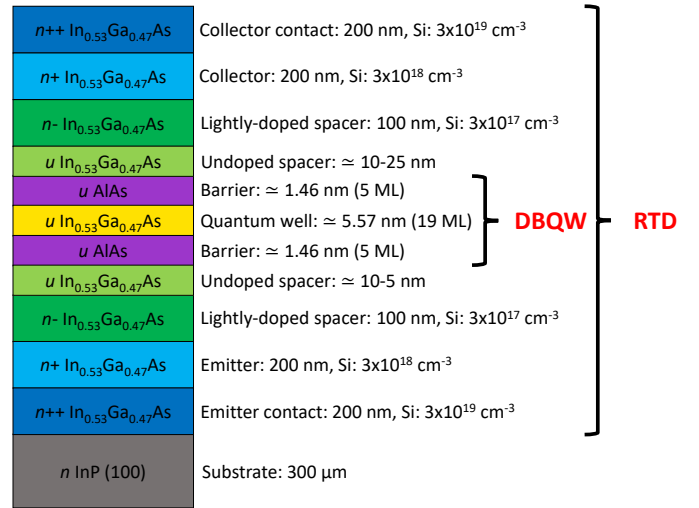

Fig. 1. Epitaxial structures under test (ESUT), indicating layers name, thickness, and doping level. The DBQW region is highlighted. ML stands for monolayer (1 ML $\simeq$ 0.293 nm). Layers nomenclature assumes the top contact to be forward biased with respect to the bottom one.

double-barrier quantum well (DBQW) heterostructure, featuring moderate AlAs barrier thickness ($\simeq$ 1.46 nm) and a $\simeq$ 5.57 nm thick $In_{0.53}Ga_{0.47}As$ quantum well (QW). Outside of the active region, undoped and thick lightly-doped (100 nm, Si: $N_D = 3\times10^{17}$ cm^{-3}) spacer layers, emitter and collector regions (200 nm, Si: $N_D = 3\times10^{18}$ cm^{-3}), and heavily-doped contact layers (200 nm, Si: $N_D = 3\times10^{19}$ cm^{-3}) complete the heterostructures (where Si stands for silicon (donor atom), while N_D is the associated doping concentration), which only differ in the undoped spacer layers thickness: the ESUT #2 emitter and collector spacers were set to 5 nm and 25 nm, respectively, while the ESUT #1 features 10 nm at both sides.

The idea behind the adopted design approach was to test the capability of the simulation software in capturing small variations in the JV characteristic due to a minor change at the epitaxial structure level. Barriers, QW, and emitter spacer layers were designed to achieve low peak voltage $V_p < 2$ V and low current density operation ($J_p < 150$ kA/cm^2), which were intended to increase the accuracy of the comparison study by reducing thermal dissipation, while the collector spacer layers were designed to increase the NDR voltage span ($\Delta V \gg 0.5$ V), which is typically the case of epi-designs that operate in the low-THz range [3].

The estimated intrinsic cut-off frequency limit $f_c \approx 1/4\tau_{in}$ of the ESUT #1 and #2 was $\simeq$ 396 GHz and $\simeq$ 601 GHz, respectively, where the estimated electron intrinsic delay time $\tau_{in} = \tau_{rtd} + \tau_t/2$ (being τ_{rtd} and τ_t the DBQW tunnelling time and transit time across the depletion regions, respectively) was $\simeq$ 0.63 ps and $\simeq$ 0.42 ps, respectively, from the simulated transmission coefficient and assuming the $In_{0.53}Ga_{0.47}As$ electron saturation velocity $v_{e,s} \sim 3 \times 10^7$ cm/s [23] [24].

B. NEGF simulation approach based on Atlas TCAD

In order to simulate the ESUT, a simulation deck was created and subdivided into four main parts: a) meshing and regions/electrodes definition, b) material parameters, c) models,

Compound	m_e^* $[m_0]$	m_v^* $[m_0]$	E_g [eV]	N_c [cm^{-3}]	N_v [cm^{-3}]	n_i [cm^{-3}]	χ_e [eV]	$\epsilon_{r,0}$ [ϵ_0]	$\mu_{e,l}$ [cm^{2}V^{-1}s^{-1}]
In$_{0.53}$Ga$_{0.47}$As	0.041	0.467	0.738	2.12×10^{17}	8.01×10^{18}	8.24×10^{11}	4.55	13.9	2.52×10^4
AlAs	0.146	0.79	2.153	1.50×10^{19}	1.76×10^{19}	13	3.50	10.1	1.85×10^2

* In the above, m_e^* is the electron effective mass, m_v^* is the valence band density of states effective mass, $m_0 \sim 9.109 \times 10^{-31}$ kg is the electron mass at rest, E_g is the energy band gap, N_c is the conduction band effective density of states, N_v is the valence band effective density of states, n_i is the intrinsic carriers concentration, χ_e is the electron affinity, $\epsilon_{r,0}$ is the static relative dielectric constant, $\epsilon_0 \sim 8.854 \times 10^{-12}$ F/m is the vacuum permittivity, while $\mu_{e,l}$ is the low-field electron mobility.

and d) computation. In order to achieve good balance between computational cost and simulation accuracy, the spatial mesh grid size was set to 0.01 nm in the non-equilibrium DBQW region and progressively increased up to 0.05 nm in the quasi-equilibrium emitter and collector extended contacts. Material parameters of In$_{0.53}$Ga$_{0.47}$As or AlAs were both taken from the literature [25]–[27] or derived and are reported in Table I, including electron m_e^* and valence band density of states m_v^* effective masses, energy gap E_g, electron affinity χ_e, static relative dielectric constant $\epsilon_{r,0}$, and low-field electron mobility $\mu_{e,l}$. In this context, In$_{0.53}$Ga$_{0.47}$As parameters were computed through Vegard's law by linearly interpolating the associated binary compounds within the virtual crystal approximation (VCA), i.e., $P(\text{In}_{0.53}\text{Ga}_{0.47}\text{As}) = (1 - x)P(\text{InAs}) + xP(\text{GaAs})$ (being $x = 0.47$), and by quadratically correcting through bowing parameters where available, being P one of the aforementioned parameters. Conduction N_c and valence band N_v effective density of states, as well as the intrinsic carrier concentration n_i, where then computed as $N_{c/v} = (4\pi m_{e/v}^* k_B T/h^2)^{3/2}$ and $n_i = \sqrt{N_c N_v} exp(-E_g/2k_B T)$, being $k_B \sim 8.617 \times 10^{-5}$ eV/K the Boltzmann constant and T the temperature, where $T = 300$ K (RT).

The approach implemented in Atlas [28] deals with NEGF heuristically by using elementary arguments, which is intended to simplify the standard theoretical treatment based on quantum-field theory and non-equilibrium quantum statistical mechanics [29]. Schrödinger's and Poisson's equations are solved in one-dimension (1D) numerically and self-consistently upon convergence given the input mesh-grid at RT through the finite element method (FEM) along the longitudinal transport direction z to compute potential, bands profile, and DBQW resonant eigenstates and associated eigenenergies. At the same time, NEGF quantum transport equations in Dyson's-like forms are iteratively and recursively solved at each bias point for both the retarded and lesser Green's functions G^R and $G^<$, respectively, starting from thermal equilibrium (initial guess). In this context, G^R carries information on the local density of states (LDOS) and transmission coefficient, while $G^<$ on electron and current densities, at a specific voltage, where the Fermi-Dirac distribution was adopted to model carrier statistics. Since transport is 1D ($\mathbf{k} = k_z\hat{z}$), electron and current densities are obtained by analytically integrating over the transverse plane $\mathbf{k}_\parallel = k_x\hat{x} + k_y\hat{y}$. Moreover, since current density is computed at a quantum level, the continuity equation is solved for the potential only.

At the moment, the software does not account for any scattering mechanisms and assumes ballistic transport. In this limit, the electron is represented through a single-particle pure-state wave-function which keeps phase coherence over the entire device length, i.e., the eigenstate does not change its energy and momentum during its space/time evolution. Therefore, the NEGF density matrix-like mixed-state description is simplified to a single-particle Schrödinger's equation. As a consequence, the only implemented self-energies are the retarded and less-than boundary self-energies $\Sigma_{e,c}^R$ and $\Sigma_{e,c}^<$, respectively, which are folded into the device Hamiltonian and model the semi-infinite emitter and collector contacts, as well as the openness of the system. In particular, while $\Sigma_{e,c}^R$ carries information on the contacts LDOS, $\Sigma_{e,c}^<$ accounts for their carrier statistics. In this context, Dirichlet boundary conditions are set for the potential (Ohmic contacts), while open-boundary conditions are set for carriers, which are numerically implemented within the quantum transmitting boundary method (QTBM) [30]. Further information about the NEGF solver implemented in Atlas can be found in [28].

To simplify the electronic band structure treatment, the single-band effective mass approximation was adopted to compute the dispersion relation in the conduction band (CB). This avoids computationally expensive multi-band approaches needed to account for band warping and band non-parabolicity around CB minima [31] caused by conduction-to-valence band states coupling [32] [33] in very narrow-gap semiconductor materials (whose energy band gap $E_g < 0.5$ eV [34]), while they can be neglected otherwise without excessively losing in physical accuracy, substantially reducing the amount of required computational resources and increasing simulation efficiency. Indeed, RTD devices employed in oscillators working below ~ 300 GHz make typically use of lattice-matched to InP In$_{0.53}$Ga$_{0.47}$As [3] (whose RT $E_g \sim 0.74$ eV [25]), improving epitaxial growth quality and reproducibility levels. Moreover, strain effects in the DBQW region were neglected, which results to be a good approximation since the lattice constant mismatch between the In$_{0.53}$Ga$_{0.47}$As QW and the AlAs barriers is only ~ 3 % [35]. At the same time, the parasitic series resistance R_s was neglected in the simulations. Indeed, although the effect of R_s on the device static IV characteristic is represented by the shift of the positive differential resistance (PDR) regions along the voltage axis, we show that this is negligible for small device sizes. However, load line effects can significantly affect the IV curve at large mesa areas, as

CB edge energy profile, electron density distribution, and DBQW quasi-bound resonant states at thermal equilibrium (300 K) - ESUT #1
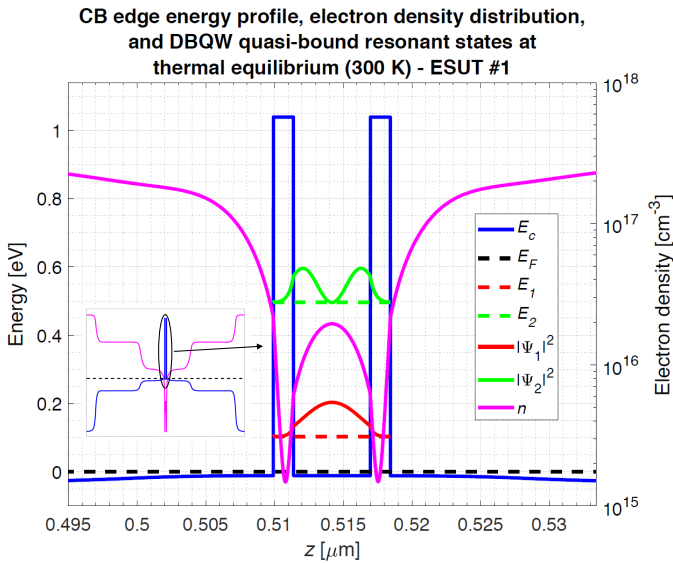

Fig. 2.   Computed CB edge energy profile $E_c(z)$ and electron density distribution $n(z)$ of the ESUT #1 at RT (300 K) and thermal equilibrium close to the DBQW region, together with associated first and second quasi-bound resonant states (energies and envelope wave-functions), as well as a zoom out over the entire device structure. $|\Psi_i|^2$ is given in arbitrary units and E_F is the Fermi level (energy reference).

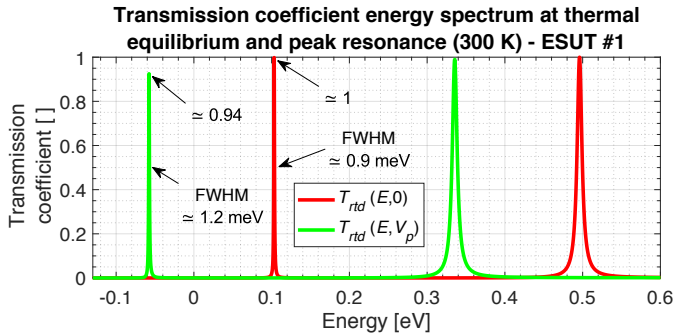**Transmission coefficient energy spectrum at thermal equilibrium and peak resonance (300 K) - ESUT #1**

Fig. 3.   Computed transmission coefficient energy spectrum (linear scale) $T_{rtd}(E,V)$ at RT (300 K) at both thermal equilibrium and peak resonance ($V=V_p$) of the ESUT #1. Peak and full-width at half maximum (FWHM) values of the resonance associated with E_1 are also shown in both conditions.

discussed in Section III−E.

The ESUT were simulated under forward bias, meaning that the device top contact (collector) was positively biased with respect to the bottom one (emitter). Indeed, RTD devices employed in low-THz oscillator sources are designed to work along one polarisation direction, typically, forward bias, so emitter and collector regions are individually designed for performance optimisation. The voltage range was set to $0-2$ V with a step of 10 mV to trade-off between numerical convergence and computational time. The simulations were carried out employing a Dell Precision 5820 workstation with the following computational capability; CPU: Intel Core i9-10900X, RAM: 32 GB DDR4. The simulation time was around 4 h and 50 min for the ESUT #1, and around 5 h and 35 min for the ESUT #2, which corresponds to around 1 min and 27 s, and 1 min and 40 s per bias point, respectively.

From an n-type intraband RTD epitaxial design perspective, RT information on the CB edge energy profile, electron density

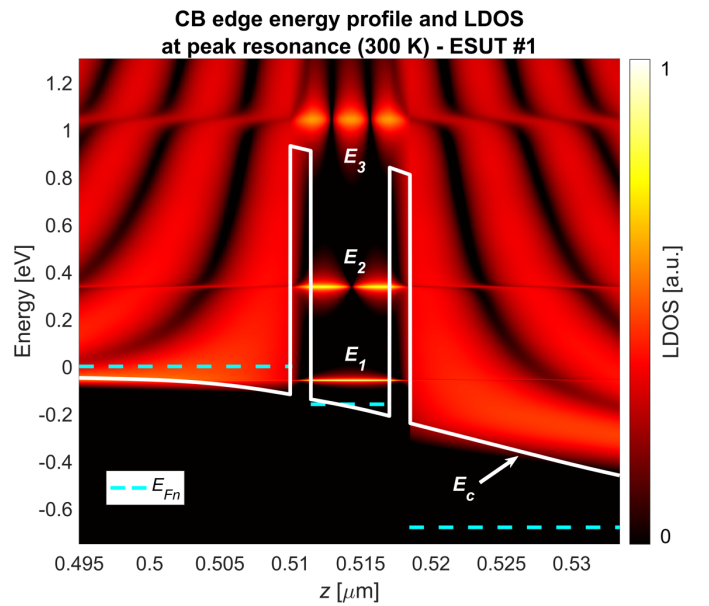**CB edge energy profile and LDOS at peak resonance (300 K) - ESUT #1**

Fig. 4.   Computed CB edge energy profile $E_c(z)$ and LDOS (log scale) of the ESUT #1 at RT (300 K) at peak resonance ($V=V_p$) close to the DBQW region, revealing the first (E_1) and second (E_2) quasi-bound resonant states, as well as the third (E_3) state (unbound). E_{Fn} is the electron quasi-Fermi level at the emitter and collector boundaries, as well as at the QW middle point.

distribution, DBQW quasi-bound resonant states, and transmission coefficient energy spectrum at thermal equilibrium and under non-equilibrium conditions are required, together with the static JV characteristic. Moreover, information about the LDOS in proximity to the DBQW region is also of interest. For instance, Fig. 2, Fig. 3, and Fig. 4 show some of these quantities computed by simulating the ESUT #1, such as the CB edge energy profile E_c (Γ point), electron density n, and transmission coefficient T_{rtd} at RT and thermal equilibrium close to the DBQW region, as well as first ($i = 1$) and second ($i = 2$) quasi-bound states resonant energy levels E_i and corresponding wave-function square modulus $|\Psi_i|^2$, where $E_i = E_{i,z}$ and $\Psi_i = \Psi_{i,z}$ are the longitudinal components associated to the bottom of the corresponding subbands. Furthermore, T_{rtd} and the LDOS are also shown at peak resonance ($V = V_p$). This information provides insight to the device operation and a basis to device design that gives a desired JV characteristic.

C. RTD devices fabrication and DC characterisation

The ESUT were grown through MBE at $T = 475$ °C on 2" sulfur (S) doped n-type (100) oriented InP substrates with thickness of ~ 300 μm. Arsine (AsH$_3$) was employed as gas precursor for arsenic (As), while emitter and collector extended contacts doping was carried out by using Si atoms.

RTD devices with square top mesa area $A = 3{\times}3$ μm^2, $4{\times}4$ μm^2, $5{\times}5$ μm^2, $6{\times}6$ μm^2, and $7{\times}7$ μm^2 were then fabricated through low-cost optical lithography on the grown wafers except from the top contacts, which were patterned through electron-beam lithography (EBL) for accurate shaping of the smaller devices, for a total of six lithographic steps. Contacts based on a titanium/palladium/gold metal stack

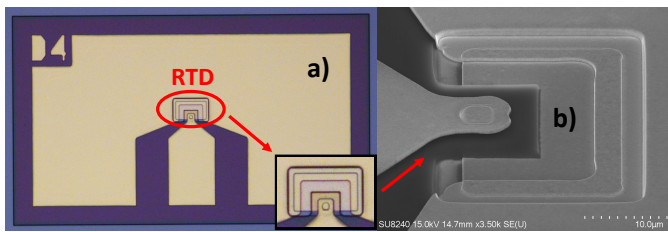| ESUT	$J_{p,s}$ [kA/cm^2]	$J_{v,s}$ [kA/cm^2]	$V_{p,s}$ [V]	$V_{v,s}$ [V]	ΔV_s [V]	$J_{p,m}$ [kA/cm^2]	$J_{v,m}$ [kA/cm^2]	$V_{v,m}$ [V]	A [μm^2]	$V_{p,m}$ [V]	ΔV_m [V]
#1	63	2	0.68	1.38	0.70	60	11	1.32	3×3	0.69	0.63
									4×4	0.71	0.61
									5×5	0.72	0.60
									6×6	0.74	0.58
									7×7	0.76	0.56
#2	110	5	0.86	1.57	0.71	108	22	1.50	3×3	0.86	0.64
									4×4	0.86	0.64
									5×5	0.87	0.63
									6×6	0.88	0.62
									7×7	0.90	0.60

* In the above, s and m subscripts indicate simulated and measured quantities, respectively.

Fig. 5. In a), a photomicrograph of a fabricated 4×4 μm^2 large RTD device, as well as a zoom in over the RTD region. In b), an SEM image zoom in over the opened via.

(Ti/Pd/Au=20/30/150 nm) and bond-pads (Ti/Au=20/400 nm) were deposited through electron-beam physical vapour deposition (EB−PVD) and dual lift-off, while device mesas were defined through anisotropic chemical wet etching (H_3PO_4:H_2O_2:H_2O=1:1:38) with rate ∼ 100 nm/min, where the associated lateral undercut σ was estimated to be $\simeq 460$ nm and $\simeq 490$ nm per mesa side for the ESUT #1 and #2, respectively, through accurate scanning electron microscopy (SEM) inspection. The emitter and collector layer surfaces were treated prior to metal evaporation through a basic ex-situ de-oxidation cleaning procedure based on ozone (O_3) atmosphere exposure under UV light for 4 min and 30 s, followed by a dip in a hydrochloric acid-based dilute solution (HCl:H_2O=1:3) for 5 min. The specific contact resistivity ρ_c was estimated to be $\simeq 1.3 \times 10^{-7} \, \Omega \, \mathrm{cm}^2 = 13 \, \Omega \, \mu\mathrm{m}^2$ for both fabricated samples and was extracted through transfer length model (TLM) measurements. Device passivation and contacts/substrate insulation were carried out using a Polyimide-based resin (PI−2545). To allow device biasing, via opening was then performed on the RTD top contact through reactive ion etching (RIE) in a tetrafluoromethane/oxygen (CF_4/O_2)-based plasma. A photomicrograph and an SEM image of a fabricated 4×4 μm^2 large RTD device are shown in Fig. 5.

The fabricated devices were then measured at RT and under forward bias (collector positively biased with respect to the emitter) through a DC sweep analysis within the voltage range $0 - 2$ V with step 10 mV by using a B1500A Semiconductor Device Parameter Analyzer from Keysight Technologies in order to retrieve the experimental static *IV* characteristics.
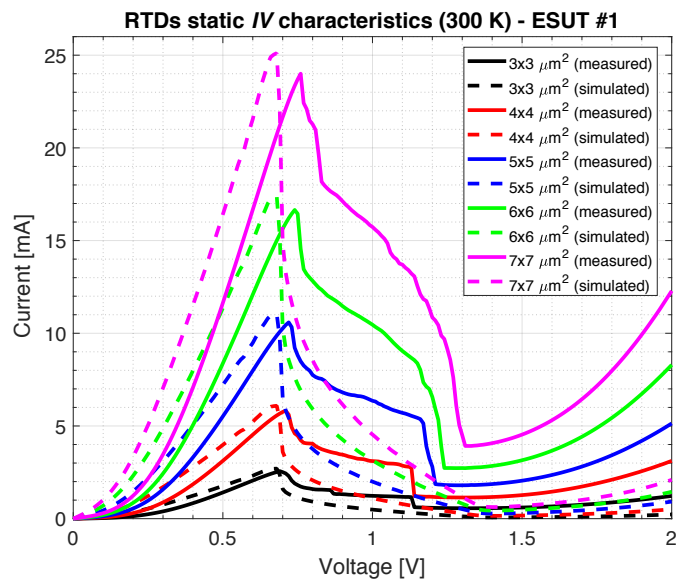

Fig. 6. Comparison between simulated and measured static *IV* characteristics at RT (300 K) and under forward bias of the RTD devices featuring the ESUT #1.

D. Simulations versus experimental results: comparison and discussion

Fig. 6 and Fig. 7 compare the simulated with the measured static *IV* characteristics of the fabricated ESUT #1 and #2 RTD devices at RT and under forward bias, respectively. Several devices per mesa area, randomly distributed across the whole samples (∼ 1.2 cm^2 large), were measured to achieve statistical significance, and no difference in their electrical properties was revealed, confirming the high wafer structural uniformity achieved during the growth process. The simulated curves are smooth in the NDR region, while the measured ones show the typical plateau in the NDR region due to low-frequency parasitic bias oscillations [36]. Simulated and experimentally extracted electrical quantities of the ESUT #1 and #2, and related RTD devices, including J_p, J_v, V_p, V_v, and ΔV, are reported in Table II.

1) J_p and J_v: the computed $J_{p,s}$ and $J_{v,s}$ of the ESUT #1 were $\simeq 63$ kA/cm^2 and $\simeq 2$ kA/cm^2, respectively, while the
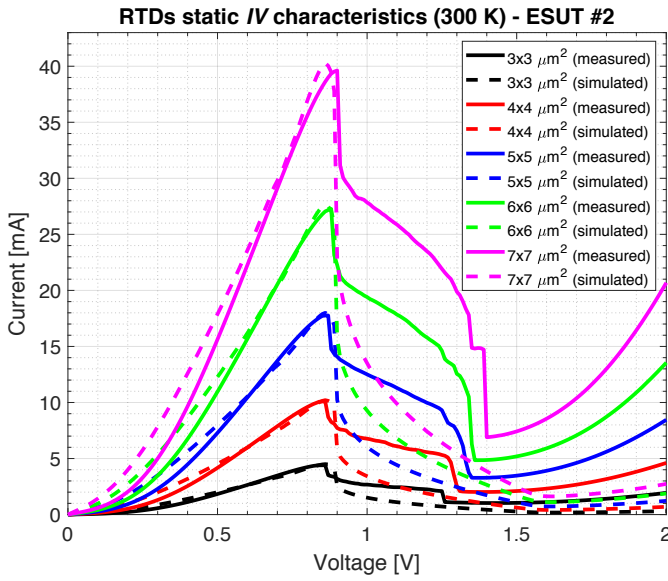
Fig. 7. Comparison between simulated and measured static *IV* characteristics at RT (300 K) and under forward bias of the RTD devices featuring the ESUT #2.
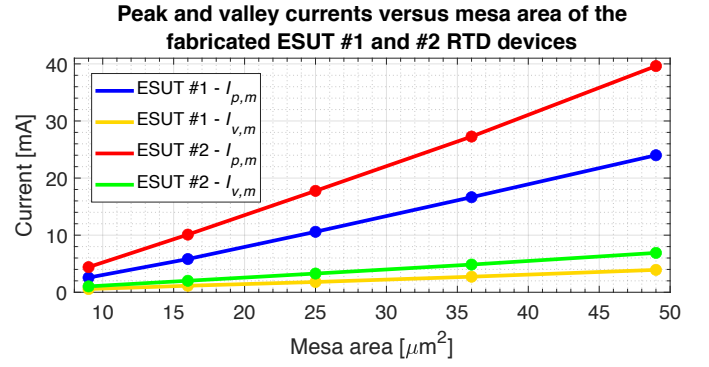

Fig. 8. Experimentally extracted ESUT #1 and #2 RTD devices peak and valley currents $I_{p,m}$ and $I_{v,m}$ as a function of the designed mesa area.
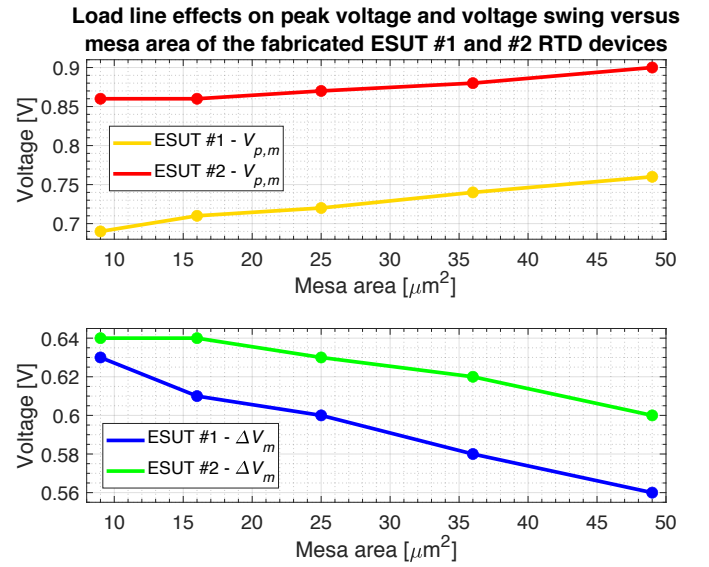

Fig. 9. Experimentally extracted ESUT #1 and #2 RTD devices peak voltage $V_{p,m}$ and voltage swing ΔV_m versus designed mesa area trends due to load line effects.

experimentally extracted $J_{p,m}$ and $J_{v,m}$ were $\simeq 60$ kA/cm^2 and $\simeq 11$ kA/cm^2, respectively, after correcting the devices top mesa areas due to anisotropic wet etch. On the other hand, the ESUT #2 values were $J_{p,s} \simeq 110$ kA/cm^2, $J_{p,m} \simeq 108$ kA/cm^2, $J_{v,s} \simeq 5$ kA/cm^2, and $J_{v,m} \simeq 22$ kA/cm^2. This resulted in a computed available current density $\Delta J_s = J_{p,s} - J_{v,s}$ and peak-to-valley current ratio PVCR$_s = J_{p,s}/J_{v,s}$ of $\simeq 61$ kA/cm^2 and $\simeq 31.5$, respectively, for the ESUT #1, and of $\simeq 105$ kA/cm^2 and $\simeq 22$, respectively, for the ESUT #2, while the extracted experimental values were $\Delta J_m \simeq 49$ kA/cm^2 and PVCR$_m \simeq 5.5$, respectively, for the ESUT #1, and $\simeq 86$ kA/cm^2 and $\simeq 4.9$, respectively, for the ESUT #2. To accurately extract $J_{p,m}$ and $J_{v,m}$, the behaviour of the experimentally measured peak and valley currents $I_{p,m}$ and $I_{v,m}$ as a function of the RTD mesa area was analysed for both heterostructures, which is shown in Fig. 8. The analysis revealed a highly linear trend, with associated maximum deviation from linearity of ~ 4.5 % for both the ESUT #1 and #2, confirming the linear dependencies $I_{p,v}(A)$ and proving that the mesa lateral sidewall leakage current contribution was negligible in the measured RTD devices.

The small overestimation of $J_{p,s}$ ($\lesssim 5$ %) and large underestimation of $J_{v,s}$ ($J_{v,m}/J_{v,s} \sim 5$), with resulting overestimations of both ΔJ_s (~ 23 %) and PVCR$_s$ (PVCR$_s$/PVCR$_m \sim 5$), can be explained by the ballistic nature of the simulations, which neglects dissipative inelastic scattering mechanisms occurring in the emitter and collector extended regions [22] [37]$-$[39]. Indeed, it has been reported that most of the valley current is not thermally activated, but it is rather associated with scattering phenomena caused by structural imperfections introduced during the epitaxial growth process of the RTD heterostructures [40], which broaden E_2 by increasing the associated transmission coefficient resonant peak full-width at half maximum (FWHM) Γ_2, increasing the current that can flow through the resonant state, enhancing J_v [15] [22] [41].

In summary, our work shows that, while simulated and measured J_p values are in very good agreement, at the moment, J_v, and therefore ΔJ and PVCR, cannot be accurately computed.

2) V_p, V_v, and ΔV: the computed and experimentally extracted V_p, V_v, and ΔV values of both the ESUT #1 and #2 RTD devices are reported in Table II. $V_{p,s}$ was computed very accurately for the small 3×3 μm^2 large devices, with 10 mV underestimation only (~ 1.5 %) in the case of the ESUT #1, which can be attributed to a small positive fluctuation in ρ_c during fabrication or/and to the absence of inelastic scattering mechanisms in the simulation [8]. Simultaneously, ΔV_s was also estimated quite accurately for the same mesa size, with ~ 11 % overestimation only (~ 70 mV). This can be explained by the absence of dissipative processes in the simulation, which increases Γ_2 and makes the voltage associated with the onset of the valley current $V_{v,m}$ to shift to lower values, shrinking the measured NDR region [42]. Indeed, the overestimation of ΔV_s is mainly due to the overestimated $V_{v,s}$ (~ 4.5 %), which it is correlated to the underestimation of $J_{v,s}$.

The mesa area trend of both $V_{p,m}$ and ΔV_m for larger device

TABLE III
EXTRACTED RTD DEVICES LOAD-LINE PARAMETERS

ESUT	A [μm^2]	R_c/R_p	R_{rtd}^*/R_s
	3×3	15.0	84.0
	4×4	6.5	79.5
#1	5×5	3.5	73.0
	6×6	2.5	59.6
	7×7	1.5	57.8
	3×3	16.0	57.4
	4×4	7.0	53.8
#2	5×5	4.0	48.8
	6×6	2.5	44.9
	7×7	1.5	43.6

* Computed assuming $R_{rtd}(V) = \bar{R}_{rtd}$ in the first PDR region.

sizes is shown in Fig. 9. It is clear that $V_{p,m}$ shifts at higher voltage with increasing mesa area, resulting in $V_{p,m}$ increasing and ΔV_m shrinking. Indeed, when the device is biased within its first PDR region, the measured voltage lies across the series of R_s and the RTD resistance $R_{rtd}(V) = dV/dI$. If $R_s \neq 0$, the measured PDR region points shift at higher voltage values according to the ratio R_{rtd}/R_s due to the parasitic voltage drop across R_s, resulting in a higher and smaller measured $V_{p,m}$ and ΔV_m, respectively. From Table III, it is clear that, while this effect is negligible for the 3×3 μm^2 large devices (where the ratio $R_{rtd}/R_s \simeq 84.0$ and $\simeq 57.4$ for the ESUT #1 and #2, respectively), as the mesa area increases, R_{rtd}/R_s decreases. Indeed, while R_{rtd} linearly scales with A, R_s doesn't follow the same trend due to the parasitic resistance R_p mainly coming from the bond-pads metallisation (where R_p was estimated to be $\simeq 0.2$ Ω for the fabricated RTD devices), i.e., $R_s \approx R_p + R_c$, where R_c is the device parasitic contact resistance. In this context, $R_c = R_{c,t} + R_{c,b} = \rho_c/(A + A_b)$ (being $R_{c,t}$ and $R_{c,b}$ are the contact resistances associated with the RTD top and bottom Ohmic contacts, respectively, while A_b is the bottom contact area), where $R_c \approx R_{c,t} = \rho_c A$ since the ratio $R_{c,t}/R_{c,b} = A_b/A$ was estimated to be ~ 22 for the fabricated devices. While the influence of R_p on R_s is negligible for the 3×3 μm^2 large devices, where $R_c/R_p \simeq 15.0$ and $\simeq 16.0$ for the ESUT #1 and #2, respectively, the ratio decreases for the bigger mesa areas. Therefore, the ratio R_{rtd}/R_s, in turn, drops. As a consequence, the NDR shrinks according to the load line slope [43]. If $R_s = 1/|\bar{G}_{rtd}|$, where $\bar{G}_{rtd} < 0$ is the RTD negative differential conductance (NDC), the device becomes extrinsically bistable, i.e., $V_p = V_v$, and the NDR vanishes, meaning that the RTD cannot be biased in this region.

In summary, our analysis shows that both V_p and ΔV can be accurately computed for the 3×3 μm^2 large RTD devices, being the simulation offset < 0.1 V, which is the tolerance that is usually adopted to quantify these parameters during wafer qualification. However, the estimation is not that accurate in the case of the larger area devices due to load-line effects. Therefore, small device sizes should be employed to correctly carry out accurate wafer qualification and estimate the associated V_p and ΔV when the experimental RTD IV

characteristics are measured. Suitable mesa areas must be chosen according to the wafer electrical properties and the Ohmic specific contact resistivity achieved during device fabrication. It is also clear that load-line effects alter the electrical behaviour of large device sizes. Therefore, even though both V_p and ΔV are intimately related with the RTD epitaxial-structure, R_s can mask the real wafer electrical performance if the measured devices are not sufficiently small, leading to poor qualification.

3) $P_{RF,max}$: the experimentally estimated $P_{RF,max,m} \approx (3/16)\Delta J\Delta V$ was $\simeq 0.06$ mW/μm^2 for the ESUT #1 and $\simeq 0.1$ mW/μm^2 for the ESUT #2, while the estimated counterpart from simulations $P_{RF,max,s}$ was $\simeq 0.08$ mW/μm^2 and $\simeq 0.14$ mW/μm^2, respectively, with a discrepancy of around $\sim 30-40$ % due to the underestimated valley current density $J_{v,s}$, as already discussed. This means that a 16 μm^2 large RTD device can theoretically deliver up to $\simeq 1$ mW and $\simeq 1.6$ mW of RF power featuring the ESUT #1 or #2, respectively.

Clearly, this value can be well increased through accurate device epitaxial structure design. In particular, barriers and QW thicknesses have to be optimised to achieve moderate current density operation, i.e., $150 < J_p < 250$ kA/cm^2, and large PVCR > 3, resulting in $\Delta J \gg 100$ kA/cm^2. This allows the employment of large mesa areas $A \geq 9$ μm^2 required for high-power operation without suffering from thermal breakdown issues. At the same time, emitter and collector spacer layers thicknesses and doping levels have to be optimised to maximise the NDR voltage swing ΔV above 1 V and keep moderate V_p below 2 V to minimise DC power consumption. For instance, assuming an RTD heterostructure featuring $J_p = 250$ kA/cm^2, PVCR $= 5$, $\Delta J = 200$ kA/cm^2, and $\Delta V = 1$ V, a 16 μm^2 large device can deliver up to ~ 6 mW of RF power, which represents an around 4-fold improvement compared to this work.

IV. CONCLUSIONS

We demonstrated a simulation approach based on the NEGF method implemented in SILVACO Inc. Atlas TCAD simulation package to accurately estimate the static JV characteristic of lattice-matched to InP In$_{0.53}$Ga$_{0.47}$As/AlAs double-barrier RTD heterostructures. We showed that the peak current density J_p, peak voltage V_p, and the NDR voltage extent ΔV can be accurately estimated. Currently, the valley current density J_v, and so the available current density ΔJ and peak-to-valley current ratio PVCR, cannot be correctly computed due to the lack of dissipative processes, which will be included in a future release of the software and allow to fully model the JV curve.

We conclude that the demonstrated simulation approach can be employed to design and optimise RTD devices through the associated IV curve, and will assist in leveraging the RTD oscillator output power beyond the 1 mW threshold in the low-THz band towards levels needed for practical applications. Future work will consist in maximising $P_{RF,max}$ through epitaxial structure design simulations and investigating the reliability of the simulation software in estimating the RTD heterostructure capacitance C_{rtd} and QW inductance L_{qw}, providing a complete high-frequency equivalent circuit compact model.

V. ACKNOWLEDGMENTS

The authors would like to thank the James Watt Nanofabrication Centre (JWNC) staff, University of Glasgow, for the support during devices fabrication.

REFERENCES

[1] D. Cimbri, J. Wang, A. Al-Khalidi, and E. Wasige, "Resonant Tunnelling Diode High-Speed Terahartz Wireless Communications - A Review," *IEEE Transactions on Terahertz Science and Technology*, vol. 12, no. 3, pp. 226-244, 2022, doi: 10.1109/TTHZ.2022.3142965.

[2] T. Miyamoto, A. Yamaguchi, and T. Mukai, "Terahertz imaging system with resonant tunneling diodes," *Japanese Journal of Applied Physics*, vol. 55, no. 3, pp. 032201, 2016, doi: 10.7567/jjap.55.032201.

[3] A. Al-Khalidi, K. H. Alharbi, J. Wang, R. Morariu, L. Wang, A. Khalid, J. M. L. Figueiredo, and E. Wasige, "Resonant Tunneling Diode Terahertz Sources With up to 1 mW Output Power in the J-Band," *IEEE Transactions on Terahertz Science and Technology*, vol. 10, no. 2, pp. 150-157, 2020, doi: 10.1109/TTHZ.2019.2959210.

[4] J. Wang, A. Al-Khalidi, S. Ahearne, and E. Wasige, "1080P HD video transmission using RTD transmitter," *14th UK-Europe-China Workshop on Millimetre-Waves and Terahertz Technologies (UCMMT)*, pp. 1-3, 2021, doi: 10.1109/UCMMT53364.2021.9569915.

[5] P. Smulders, "The road to 100 Gb/s wireless and beyond: basic issues and key directions," *IEEE Communications Magazine*, vol. 51, no. 12, pp. 86-91, 2013, doi: 10.1109/MCOM.2013.6685762.

[6] C. Kim and A. Brandli, "High-Frequency High-Power Operation of Tunnel Diodes," *IRE Transactions on Circuit Theory*, vol. 8, no. 4, pp. 416-425, 1961, doi: 10.1109/TCT.1961.1086849.

[7] G. Klimeck, "Quantum and Semi-Classical Transport in NEMO 1-D," *Journal of Computational Electronics*, vol. 2, no. 2, pp. 177-182, 2003, doi: 10.1023/B:JCEL.0000011421.53762.97.

[8] T. Kubis and P. Vogl, "Self-consistent quantum transport theory: Applications and assessment of approximate models," *Journal of Computational Electronics*, vol. 6, no. 1, pp. 183-186, 2007, doi: 10.1007/s10825-006-0078-6.

[9] C. P. Allford and P. D. Buckle, "Strain Compensated InGaAs/AlAs Triple Barrier Resonant Tunneling Structures for THz Applications," *IEEE Transactions on Terahertz Science and Technology*, vol. 7, no. 6, pp. 772-779, 2017, doi: 10.1109/TTHZ.2017.2758266.

[10] W. M. Jubadi, M. A. Md Zawawi, and M. Missous, "Simulative study on physical modelling of submicrometer highly-strained $In_{0.8}Ga_{0.2}As$/AlAs resonant tunnelling diode," *The Tenth International Conference on Advanced Semiconductor Devices and Microsystems*, pp. 1-4, 2014, doi: 10.1109/ASDAM.2014.6998671.

[11] A. Alqurashi and M. Missous, "Physical Modeling of Asymmetric Spacers Resonant Tunneling Diodes (RTDs)," *IEEE Latin America Electron Devices Conference (LAEDC)*, pp. 1-4, 2021, doi: 10.1109/LAEDC51812.2021.9437970.

[12] D. R. Celino, A. M. de Souza, C. L. M. P. Plazas, R. Ragi, and M. A. Romero, "Fully Analytical Compact Model for the I-V Characteristics of Resonant Tunneling Diodes," *35th Symposium on Microelectronics Technology and Devices (SBMicro)*, pp. 1-4, 2021, doi: 10.1109/SBMicro50945.2021.9585749.

[13] J. N. Schulman, H. J. De Los Santos, and D. H. Chow, "Physics-based RTD current-voltage equation," *IEEE Electron Device Letters*, vol. 17, no. 5, pp. 220-222, 1996, doi: 10.1109/55.491835.

[14] E. R. Brown, "High-Speed Resonant-Tunneling Diodes," in *VLSI Electronics Microstructure Science*, chapter 10, vol. 24, pp. 305-350, 1994, doi: 10.1016/B978-0-12-234124-3.50015-X.

[15] H. Ohnishi, T. Inata, S. Muto, N. Yokoyama, and A. Shibatomi, "Self-consistent analysis of resonant tunneling current," *Applied Physics Letters*, vol. 49, no. 19, pp. 1248-1250, 1986, doi: 10.1063/1.97428.

[16] J. P. Sun, G. I. Haddad, P. Mazumder, and J. N. Schulman, "Resonant tunneling diodes: models and properties," *Proceedings of the IEEE*, vol. 86, no. 4, pp. 641-660, 1998, doi: 10.1109/5.663541.

[17] P. Roblin and W. -R. Liou, "Three-dimensional scattering-assisted tunneling in resonant-tunneling diodes," *Physical Review B*, vol. 47, no. 4, pp. 2146-2161, 1999, doi: 10.1103/PhysRevB.47.2146.

[18] S. Datta, "Lessons from Nanoelectronics: A New Perspective on Transport − Part B: Quantum Transport," World Scientific, 2018, doi: 10.1142/10440-vol2.

[19] S. Datta, "Nanoscale device modeling: the Green's function method," *Superlattices and Microstructures*, vol. 28, no. 4, pp. 253-278, 2000, doi: 10.1006/spmi.2000.0920.

[20] R. Lake, G. Klimeck, R. C. Bowen, and D. Jovanovic, "Single and multiband modeling of quantum electron transport through layered semiconductor devices," *Journal of Applied Physics*, vol. 81, no. 12, pp. 7845-7869, 1997, doi: 10.1063/1.365394.

[21] L. Shifren, C. Ringhofer, and D. K. Ferry, "A Wigner function-based quantum ensemble Monte Carlo study of a resonant tunneling diode," *IEEE Transactions on Electron Devices*, vol. 50, no. 3, pp. 769-773, 2003, doi: 10.1109/TED.2003.809434.

[22] R. Lake and S. Datta, "Nonequilibrium Green's-function method applied to double-barrier resonant-tunneling diodes," *Physical Review B*, vol. 45, no. 12, pp. 6670-6685, 1992, doi: 10.1103/PhysRevB.45.6670.

[23] M. Asada, S. Suzuki, and N. Kishimoto, "Resonant Tunneling Diodes for Sub-Terahertz and Terahertz Oscillators," *Japanese Journal of Applied Physics*, vol. 47, no. 6R, pp. 4375-4384, 2008, doi: 10.1143/JJAP.47.4375.

[24] H. Kanaya, T. Maekawa, S. Suzuki, and M. Asada, "Structure dependence of oscillation characteristics of resonant-tunneling-diode terahertz oscillators associated with intrinsic and extrinsic delay times," *Japanese Journal of Applied Physics*, vol. 54, no. 9, pp. 094103, 2015, doi: 10.7567/JJAP.54.094103.

[25] M. Levinshtein, S. Rumyantsev, and M. Shur, "Handbook Series on Semiconductor Parameters: Volume 1 and 2," *World Scientific*, 1996, doi: 10.1142/2046.

[26] O. Madelung, "Semiconductors: Data Handbook," *Springer*, 2004, doi: 10.1007/978-3-642-18865-7.

[27] I. Vurgaftman, J. R. Meyer, and L. R. Ram-Mohan, "Band parameters for III-V compound semiconductors and their alloys," *Journal of Applied Physics*, vol. 89, no. 11, pp. 5815-5875, 2001, doi: 10.1063/1.1368156.

[28] Atlas User's Manual: Device Simulation Software, Silvaco Inc., 2016.

[29] K. Y. Camsari, S. Chowdhury, and S. Datta, "The Non-Equilibrium Green Function (NEGF) Method," 2021, doi: 10.48550/arXiv.2008.01275.

[30] N. G. Einspruch and W. R. Frensley, "Heterostructures and Quantum Devices," *Academic Press*, 1994.

[31] G. Klimeck, R. C. Bowen, T. B. Boykin, and T. A. Cwik, "sp3s* Tight-binding parameters for transport simulations in compound semiconductors," *Superlattices and Microstructures*, vol. 27, no. 5-6, pp. 519-524, 2000, doi: 10.1006/spmi.2000.0862.

[32] G. Liu and S. -L. Chuang, "Modeling of Sb-based type-II quantum cascade lasers," *Physical Review B*, vol. 65, no. 16, pp. 165220, 2002, doi: 10.1103/PhysRevB.65.165220.

[33] T. B. Bahder, "Eight-band k·p model of strained zinc-blende crystals," *Physical Review B*, vol. 41, no. 17, pp. 11992-12001, 1990, doi: 10.1103/PhysRevB.41.11992.

[34] E. O. Kane, "Band structure of indium antimonide," *Journal of Physics and Chemistry of Solids*, vol. 1, no. 4, pp. 249-261, 1957, doi: 10.1016/0022-3697(57)90013-6.

[35] S. C. Jain, M. Willander, and H. Maes, "Stresses and strains in epilayers, stripes and quantum structures of III - V compound semiconductors," *Semiconductor Science and Technology*, vol. 11, no. 5, pp. 641-671, 1996, doi: 10.1088/0268-1242/11/5/004.

[36] L. Wang, J. M. L. Figueiredo, C. N. Ironside, and E. Wasige, "DC Characterization of Tunnel Diodes Under Stable Non-Oscillatory Circuit Conditions," *IEEE Transactions on Electron Devices*, vol. 58, no. 2, pp. 343-347, 2011, doi: 10.1109/TED.2010.2091507.

[37] H. Kanaya, R. Sogabe, T. Maekawa, S. Suzuki, and M. Asada, "Fundamental Oscillation up to 1.42 THz in Resonant Tunneling Diodes by Optimized Collector Spacer Thickness," *Journal of Infrared, Millimeter, and Terahertz Waves*, vol. 35, no. 5, pp. 425-431, 2014, doi: 10.1007/s10762-014-0058-z.

[38] R. Lake, G. Klimeck, R. C. Bowen, C. Fernando, T. Moise, Y. C. Kao, and M. Leng, "Interface roughness, polar optical phonons, and the valley current of a resonant tunneling diode," *Superlattices and Microstructures*, vol. 20, no. 3, pp. 279-285, 1996, doi: 10.1006/spmi.1996.0079.

[39] G. Klimeck, R. Lake, and D. K. Blanks, "Role of interface roughness scattering in self-consistent resonant-tunneling-diode simulations," *Physical Review B*, vol. 58, no. 11, pp. 7279-7285, 1998, doi: 10.1103/PhysRevB.58.7279.

[40] K. J. P. Jacobs, B. J. Stevens, R. Baba, O. Wada, T. Mukai, and R. A. Hogg, "Valley current characterization of high current density resonant tunnelling diodes for terahertz-wave applications," *AIP Advances*, vol. 7, no. 10, pp. 105316, 2017, doi: 10.1063/1.4997664.

[41] N. C. Kluksdahl, A. M. Kriman, D. K. Ferry, and C. Ringhofer, "Self-consistent study of the resonant-tunneling diode," *Physical Review B*, vol. 39, no. 11, pp. 7720-7735, 1989, doi: 10.1103/PhysRevB.39.7720.

[42] J. P. Sun and G. I. Haddad, "Self-Consistent Scattering Calculation of Resonant Tunneling Diode Characteristics," *VLSI Design*, vol. 6, pp. 078412, 1998, doi: 10.1155/1998/78412.

[43] W. F. Chow, "Principles of tunnel diode circuits," Wiley, 1964.